



DiFSD: Ego-Centric Fully Sparse Paradigm with Uncertainty Denoising and Iterative Refinement for Efficient End-to-End Self-Driving

Haisheng Su^{1,2} Wei Wu² Junchi Yan¹ (✉)

¹School of AI and Department of CSE, Shanghai Jiao Tong University

²SenseAuto Research

{suhaiseng, yanjunchi}@sjtu.edu.cn, wuwei@senseauto.com

Code & Model: [SenseAuto](#) & [SJTU-ReThinkLab/DiFSD](#)

Abstract

Current end-to-end autonomous driving methods resort to unifying modular designs for various tasks (e.g. perception, prediction and planning). Although optimized in a planning-oriented spirit with a fully differentiable framework, existing end-to-end driving systems without ego-centric designs still suffer from unsatisfactory performance and inferior efficiency, owing to the rasterized scene representation learning and redundant information transmission. In this paper, we revisit the human driving behavior and propose an ego-centric fully sparse paradigm, named DiFSD, for end-to-end self-driving. Specifically, DiFSD mainly consists of sparse perception, hierarchical interaction and iterative motion planner. The sparse perception module performs detection, tracking and online mapping based on sparse representation of the driving scene. The hierarchical interaction module aims to select the Closest In-Path Vehicle / Stationary (CIPV / CIPS) from coarse to fine, benefiting from an additional geometric prior. As for the iterative motion planner, both selected interactive agents and ego-vehicle are considered for joint motion prediction, where the output multi-modal ego-trajectories are optimized in an iterative fashion. Besides, both position-level motion diffusion and trajectory-level planning denoising are introduced for uncertainty modeling, thus facilitating the training stability and convergence of the whole framework. Extensive experiments conducted on nuScenes and Bench2Drive datasets demonstrate the superior planning performance and great efficiency of DiFSD.

1. Introduction

Autonomous driving has experienced notable progress in recent years. Traditional driving systems are commonly decoupled into several standalone tasks, e.g. perception, prediction and planning. However, heavily relying on hand-crafted post-processing, the well-established modu-

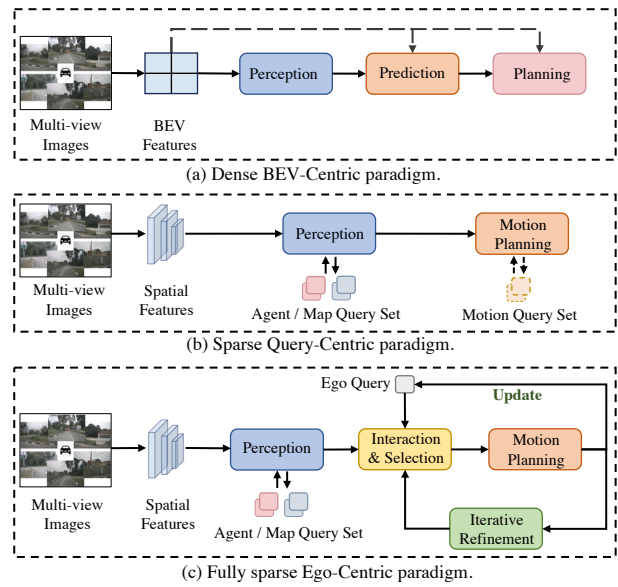


Figure 1. The comparison of different end-to-end paradigms. (a) The dense **BEV-Centric** paradigm. (b) The sparse **Query-Centric** paradigm. (c) The proposed fully sparse **Ego-Centric** paradigm.

lar systems suffer from information loss and error accumulation across sequential modules. Recently, end-to-end paradigm integrates all tasks into a unified model for planning-oriented optimization, showcasing great potential in pushing the limit of autonomous driving performance.

Literally, existing end-to-end models [11, 17, 36, 41] designed for reliable trajectory planning can be classified into two mainstreams as summarized in Fig. 1(a) and (b). The dense BEV-Centric paradigm [11, 41] performs perception, prediction and planning consecutively upon the shared BEV (Bird’s Eye View) features, which are computationally expensive leading to inferior efficiency. The sparse Query-Centric paradigm [36] utilizes sparse representation to achieve scene understanding and joint motion planning, thus improving the overall efficiency. However, object-intensive motion prediction inevitably causes computational redundancy and violates the driving habits of hu-

man drivers, who usually only concentrate on the Closest In-Path Vehicle / Stationary (CIPV / CIPS) which are more likely to affect the driving intention and trajectory planning of ego-vehicle. Meanwhile, excessive interaction with irrelevant agents will be conversely adverse to the ego-planning. Therefore, the planning performance remains unsatisfactory in both planning safety, comfort and personification.

To this end, we propose DiFSD, an Ego-Centric fully sparse paradigm as shown in Fig. 1(c). Specifically, DiFSD mainly consists of sparse perception, hierarchical interaction and iterative motion planner. In the sparse perception module, multi-scale image features extracted from visual encoder are adopted for object detection, tracking and online mapping simultaneously in a sparse manner. Then the hierarchical interaction performs ego-centric and object-centric dual interaction to select the CIPV / CIPS with the help of an additional geometric prior. Thus the interactive queries can be selected gradually from coarse to fine. As for the motion planner, the mutual information between sparse interactive queries and ego-query is considered for motion prediction in a joint decoder, which is neglected in previous methods [11, 17] but is essential especially in the scenarios like intersections. To ensure the planning rationality and selection accuracy of interactive queries, the iterative planning optimization is further applied to the multi-modal proposal ego-trajectories, through continually updating the reference line and ego-query. Moreover, both position-level motion diffusion and trajectory-level planning denoising are introduced for stable training and fast convergence. It can not only model the uncertain positions of interactive agents for motion prediction, but also enhance the quality of trajectory refinement with arbitrary offsets. With above elaborate designs, DiFSD exhibits the great potential of fully sparse paradigm for end-to-end autonomous driving, which significantly reduces the average L2 error by **56%** and collision rate by **92%** than UniAD [11] respectively. Notably, our DiFSD-S achieves **8.2** \times faster running efficiency as well. In sum, the main contributions of our work are as follows:

- We propose an ego-centric **Fully Sparse** paradigm for end-to-end self-Driving, named as **DiFSD**, without any computationally intensive dense scene representation learning and redundant environmental modeling, which is proven to be effective and efficient for ego-planning.
- We introduce a geometric prior through intention-guided attention, where the **Closest In-Path Vehicle / Stationary (CIPV / CIPS)** are gradually picked out through ego-centric cross attention and selection. Besides, both position-level diffusion of interactive agents and trajectory-level denoising of ego-vehicle are adopted for uncertainty modeling of motion planning respectively.
- Extensive experiments are conducted on nuScenes [1] and Bench2Drive [15] for both open and closed-loop planning evaluation, which demonstrate the superiority and promi-

nent efficiency of our DiFSD, revealing the great potential of the proposed ego-centric fully sparse paradigm.

2. Related Work

2.1. End-to-End Perception

Recent years witness remarkable progress achieved in multi-view 3D detection, which mainly build elaborate designs upon the dense BEV (Bird’s Eye View) or sparse query features. To generate BEV features, LSS [33] lifts 2D image features to 3D space using depth estimation results, which are then splatted into BEV plane. Follow-up works apply such operation to perform view transform for 3D detection task [7, 13, 14, 19]. Differently, some works [12, 20, 40] project a series of predefined BEV queries in 3D space to the image domain for feature sampling. As for the sparse fashion, current methods [24–27, 38] adopt a set of sparse queries to integrate spatial-temporal aggregations from multi-view image feature sequence for iterative anchor refinement.

Besides, Multi-Object Tracking (MOT) across multi-cameras is also required for downstream tasks. Recent works [32, 35, 42, 44, 46] seek to explore the joint detection and tracking methods by introducing track queries to detect the unique instances continuously. Sparse4Dv3 [24] proposes an advanced 3D detector which takes the spatial-temporal information to propagate temporal instances for identity reserving, thus achieving superior end-to-end performance without additional tracking designs.

2.2. Online Mapping

Maps could provide important static scenario information to ensure driving safety. Current works [18, 23, 28, 43] manage to construct online maps with on-board sensors, instead of using HD-Map which is labor intensive and expensive. HDMaNet [18] achieves this aim through BEV semantic segmentation and heuristic post-processing to generate map instances. VectorMapNet [28] introduces a two-stage auto-regressive transformer to refine map elements consecutively. MapTR [23] regards map elements as a set of points with equivalent permutations, while StreamMapNet [43] adopts a temporal fusion strategy to enhance the performance. However, all of them rely on dense BEV features for online map construction, which is computationally intensive and not extensible to the sparse manner.

2.3. End-to-End Motion Prediction

Motion prediction of surrounding agents in an end-to-end fashion can relieve the accumulative error between standalone models. FaF [31] predicts both current and future bounding boxes from images using a single convolution network. IntentNet [2] attempts to reason high-level behavior and long-term trajectories simultaneously. PnPNet [22]

aggregate trajectory-level features for motion prediction through an online tracking module. ViP3D [6] takes images and HD-Map as input, and adopts agent queries to conduct tracking and prediction. PIP [16] further proposes to replace HD-Map with local vectorized map.

2.4. End-to-End Planning

End-to-end planning paradigm either unites modules of perception and prediction [11, 17, 41, 47], or adopts a direct optimization on planning without intermediate tasks [3, 4, 34], which lack interpretability and are hard to optimize. Recently, UniAD [11] presents a planning-oriented model which integrates various tasks in the dense BEV-Centric paradigm, achieving convincing performance. VAD [17] learns vectorized scene representations and improves planning safety with explicit constraints. GraphAD [47] constructs the interaction scene graph to model both dynamic and static relations. SparseDrive [36] introduces the symmetric sparse perception for parallel motion planner. However, using straightforward designs and exhaustive modeling without ego-centric interaction, will inevitably lead to unsatisfactory planning performance and inferior efficiency.

3. Our Approach

3.1. Overview

The overall framework of proposed DiFSD is illustrated in Fig. 2, which deals with the end-to-end planning task in an ego-centric fully sparse paradigm. Specifically, DiFSD mainly consists of four parts: visual encoder, sparse perception, hierarchical interaction and iterative motion planner. First, the visual encoder extracts multi-scale spatial features from given multi-view images. Then the sparse perception takes the encoded features as input to perform detection, tracking and online mapping simultaneously. In the hierarchical interaction module, the ego query equipped with a geometric prior is introduced to pick out the interactive queries through ego-centric cross attention and hierarchical selection. In the iterative motion planner, both interactive agents and ego-vehicle are considered for joint motion prediction, then the predicted multi-modal ego-trajectories are further optimized iteratively. Meanwhile, both position-level diffusion of interactive agents and trajectory-level denoising of ego-vehicle are conducted for uncertainty modeling of motion and planning tasks respectively.

3.2. Problem Formulation

Given multi-view camera image sequence can be denoted as $S = \{I_t \in \mathbb{R}^{N \times 3 \times H \times W}\}_{t=T-k}^T$, where N is the number of camera views and k indicates the temporal length till current timestep T respectively. Annotation of input S for end-to-end planning is composed by a set of future waypoints of the ego-vehicle $\psi = \{\phi = (x_t, y_t)\}_{t=1}^{T_p}$, where $T_p = 3s$ is

the planning time horizon, and (x_t, y_t) is the BEV location transformed to the ego-vehicle coordinate system at current timestep T . Meanwhile, driving command as well as ego-status is also provided. Annotation set ψ is used during training. During prediction, the planned trajectory of ego-vehicle should fit the annotation ψ with minimum L2 errors and collision rate with surrounding agents.

3.3. Sparse Perception

After extracting the multi-view visual features F from sensor images using the visual encoder [8], sparse query-based perception method proposed in [24, 25] is extended to perform unified detection and online mapping in parallel with the symmetric architecture as adopted in [36].

Detection. Following the previous sparse perception methods [24, 25], surrounding agents can be represented by a group of instance features $F_a \in \mathbb{R}^{N_a \times C}$ and anchor boxes $B_a \in \mathbb{R}^{N_a \times 11}$ respectively. And each anchor box is denoted as $\{x, y, z, \ln(w), \ln(h), \ln(l), \sin(\theta), \cos(\theta), v_x, v_y, v_z\}$, which contains location, dimension, yaw angle as well as velocity respectively. Taking F_a, B_a and the visual features F as input, N_{dec} decoders are adopted to consecutively refine the anchor boxes and update the instance features through deformable aggregation of sample features projected from key points of B_a . The updated instance features are adopted to predict the classification scores and box offsets respectively. Temporal instance denoising is introduced to improve model stability.

Online Mapping. Similarly, we adopt an additional detection branch of same structure for online mapping. Differently, the geometric anchor of each static map element is denoted as N_p points. Therefore, surrounding maps can be represented by a group of map instance features $F_m \in \mathbb{R}^{N_m \times C}$ and anchor polylines $B_m \in \mathbb{R}^{N_m \times N_p \times 2}$.

3.4. Ego-Env Hierarchical Interaction

We continue to perform hierarchical interaction between the ego-vehicle and surrounding objects. As shown in Fig. 2, the hierarchical interaction module mainly consists of three parts: *Ego-Object Dual Interaction*, *Intention-guided Geometric Attention* and *Coarse-to-Fine Selection*.

Ego-Object Dual Interaction. As shown in Fig. 3, a learnable embedding $F_e \in \mathbb{R}^{1 \times C}$ is randomly initialized to serve as ego query, along with an ego anchor box $B_e \in \mathbb{R}^{1 \times 11}$ together to represent the ego-vehicle. Both ego-centric cross attention with surrounding objects $F_o \in \mathbb{R}^{N_o \times C}$ ($N_o = N_a + N_m$) and object-centric self attention are conducted consecutively to capture the mutual information comprehensively. During the attention calculation process, we combine positional embedding and query feature in a concatenated manner instead of an additive approach, which can effectively retain both semantic and geometric clues for

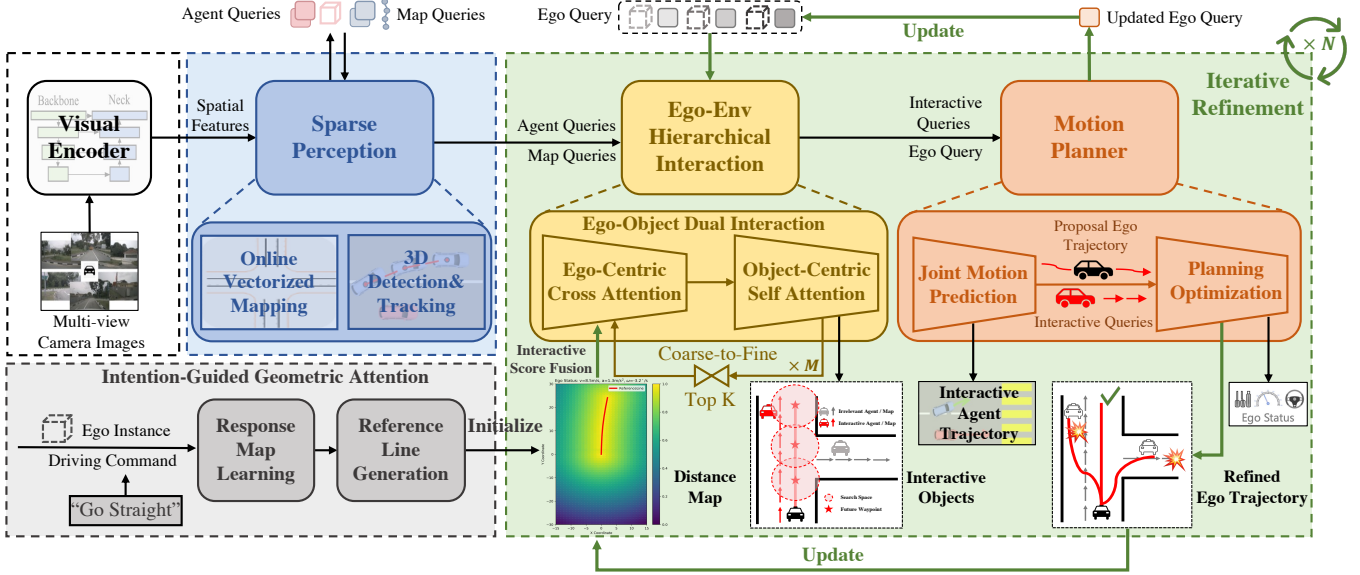


Figure 2. Overview of our proposed framework. DiFSD first extracts multi-scale image features from multi-view images using an off-the-shelf visual encoder, then perceives both dynamic and static elements in a sparse manner. The Ego-Env hierarchical interaction module is presented to select the interactive queries from coarse to fine using three different driving commands of ego queries, which are leveraged for joint motion planner through iterative refinement. An additional geometric prior is introduced for high-quality query ranking through intention-guided attention. Besides, both position-level agent diffusion and trajectory-level ego-vehicle denoising are conducted for uncertainty modeling of the end-to-end driving system.

interaction modeling.

Intention-Guided Geometric Attention. To enhance the accuracy and explainability of query ranking to facilitate selection, we introduce an ego-centric geometric prior additionally. As shown in Fig. 2, the intention-guided attention module is adopted to assess the importance of surrounding agent and map queries, which mainly consists of three steps: *Response Map Learning*, *Reference Line Generation* and *Interactive Score Fusion*.

Specifically, we use four MLPs to encode the ego-intention respectively, including velocity, acceleration, angular velocity and driving command. And then we concatenate these embeddings to obtain ego-intention features $I_e \in \mathbb{R}^{1 \times C}$, which are further concatenated with the position embeddings $F_p \in \mathbb{R}^{H \times W \times C}$ of a group of pre-defined locations $P \in \mathbb{R}^{H \times W \times 2}$ to cover densely distributed grid cells in the BEV plane. The position of each grid cell is represented as $p = (x, y)$. Finally, the concatenated geometric features are fed to a single SE [9] block to learn response map $M_r \in \mathbb{R}^{H \times W \times 1}$, which is supervised by the normalized minimum distance from p to the ego future waypoints. *The motivation is that the Closest In-Path Vehicle / Stationary are prone to affect the ego-intention, and vice versa.*

With the predicted response map M_r , we first generate the reference line through row-wise thresholding, which are further used to generate the normalized distance map M_d (See Fig. 2). Then we can obtain the geometric score S_{geo} for each surrounding query by referring to the M_d . The rea-

son why we don't get the geometric score from M_r directly is that the imbalanced distribution of ego-intention and future waypoints may lead to the inferior quality of M_r .

Finally, as shown in Fig. 4, we perform interactive score fusion through multiplying the attention, geometric and classification scores during the ego-centric cross attention:

$$S_{inter} = \underbrace{\text{Softmax}(F_e \odot F_o^T / \sqrt{d_k})}_{S_{attn} \in \mathbb{R}^{N \times 1}} \cdot S_{geo} \cdot S_{cls}, \quad (1)$$

where the distance-prior is weighted with the attention score S_{attn} for both interaction and selection. \odot is inner product, \cdot is dot product, and d_k is the channel dimension.

Coarse-to-Fine Selection. To capture the interaction information from coarse to fine, we stack M dual-interaction layers in a cascaded manner, where a top-K operation is appended between each two consecutive layers, thus the interactive objects can be gradually selected for latter prediction and planning usages. We claim that only a few interactive objects need to be considered for motion prediction, which are enough yet efficient for ego-centric path planning, instead of all detected agents existing in the driving scene.

3.5. Iterative Motion Planner

As shown in Fig. 2, the iterative motion planner is designed to conduct motion prediction for both interactive agents and ego-vehicle, and then optimize the proposal ego-trajectory with both safety and kinematic constrains iteratively.

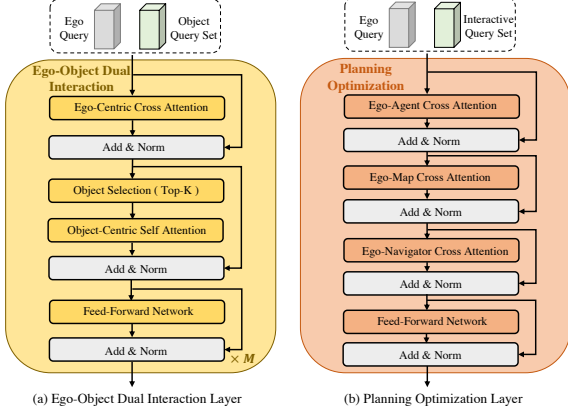


Figure 3. Illustration of the dual interaction layer in the hierarchical interaction module and planning optimization layer in the motion planner module.

Joint Motion Prediction. With regard to the trajectory prediction, both surrounding agents and ego-vehicle are adopted for motion modeling in a joint decoder, unlike previous works [11, 17, 41] which neglect the crucial interactions between near agents and ego-vehicle when making motion predictions, especially in the common scenarios like intersections. Another difference is that only the interactive objects F_{io} (CIPV) sparsely selected in the former module are considered, instead of all detected agents in the driving scene which maybe irrelevant to the ego-vehicle planning. As for the joint motion decoder, we prepare three copies of ego query F'_e to indicate different driving intentions (*i.e.*, turn left, turn right and keep forward), which are combined with F_{io} to conduct agent-level self attention and agent-map cross attention respectively. And then we concatenate these output attended features to predict multi-modal trajectories $\tau_a \in \mathbb{R}^{N_a \times K_a \times T_a \times 2}$, $\tau_e \in \mathbb{R}^{N_e \times K_e \times T_e \times 2}$ and classification scores $S_a \in \mathbb{R}^{N_a \times K_a}$, $S_e \in \mathbb{R}^{N_e \times K_e}$ for both agents and ego-vehicle, where $N_e = 3$ is the number of driving command for planning, $K_a = K_e = 6$ are the mode number, $T_a = T_e = 6$ are the future timestamps.

Planning Optimization. With the predicted multi-intention and multi-modal trajectories of ego-vehicle, we can select the most probable proposal trajectory with the input driving command and classification score S_e . As shown in Fig. 3(b), ego-agent, ego-map and ego-navigator cross attentions are conducted consecutively for planning optimization, where the offsets for each future waypoint are predicted upon the proposal trajectory respectively with several planning constraints proposed in [17] to ensure safety.

Iterative Refinement. To further promote the stability and performance of the whole end-to-end system, an additional iterative refinement strategy is proposed to continuously update the reference line and distance map M_d with refined ego trajectory as illustrated in Fig. 2, thus ensuring the interaction quality and selection accuracy of interactive queries.

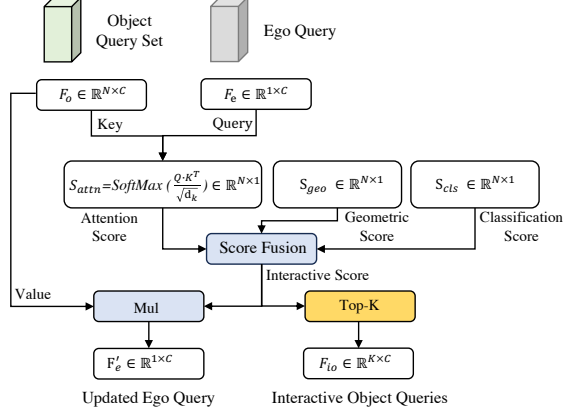


Figure 4. Details of the interactive score fusion process in the geometric attended selection.

3.6. Uncertainty Denoising

Due to the planning-oriented modular design, output uncertainty from each individual module will be inevitably introduced and passed through to the downstream tasks, leading to inferior and fragile system. Under this circumstance, we propose a two-level uncertainty modeling strategy to further stabilize the whole framework. On one hand, **position-level diffusion process** is performed on ground-truth boxes of interactive agents $B_i \in \mathbb{R}^{K \times 11}$ for additional trajectory prediction of noisy agents $B_n = B_i + \Delta B_{pos} \in \mathbb{R}^{G \times K \times 11}$ equipped with G groups of random noises following uniform distributions. ΔB_{pos} locates within two different ranges of $\{-s, s\}$ and $\{-2s, -s\} \cup \{s, 2s\}$ to indicate positives and negatives respectively, where s indicates the noise scale. This process aims to promote the stability of motion forecasting for interactive agents with uncertain detected positions, scales and velocities. On the other hand, **trajectory-level denoising process** is also introduced for robust offset prediction of proposal trajectory of ego-vehicle in the planning optimization stage. Different from the position diffusion of detection or motion query described above, we apply the random noise to trajectory offsets of ego-vehicle $\Delta B_{traj} \in \mathbb{R}^{G \times T_e \times 2}$, where s depends on the Final Displacement (FD) of ground-truth ego future trajectory.

3.7. End-to-End Learning

Multi-stage Training. To facilitate the model convergence and training performance, we divide the training process into two stages. In stage-1, the sparse perception, hierarchical interaction and joint motion prediction tasks are trained from scratch to learn sparse scene representation, interaction and motion capability respectively. Note that no selection operation is adopted in stage-1, namely all detected agents are considered for motion forecasting to make full use of annotations. In stage-2, the geometric attention module and the iterative planning optimizer are added to train

jointly for overall optimization with uncertainty modeling.

Loss Functions. The overall optimization function mainly includes five tasks, where each task can be optimized with both classification and regression losses. The overall loss function for end-to-end training can be formulated as:

$$\mathcal{L} = \mathcal{L}_{det} + \mathcal{L}_{map} + \mathcal{L}_{interact} + \sum_{i=1}^N (\mathcal{L}_{motion}^i + \mathcal{L}_{plan}^i), \quad (2)$$

where $\mathcal{L}_{interact}$ is a combination of binary classification loss and \mathcal{L}_2 regression loss to learn geometric score, where the positive (interactive) samples are denoted as grid cells with geometric score $S_{geo} \geq 0.9$ (within $3m$ for each future waypoint). An additional regression loss is included in \mathcal{L}_{plan} for ego status prediction, instead of directly using it as input to the planner as [11, 17, 41], which will lead to information leakage as proven in [21]. Meanwhile, vectorized planning constrains identified in [17] such as collision, overstepping and direction are also included in \mathcal{L}_{plan} for regularization. N is the number of motion planning stages.

4. Experiments

4.1. Datasets and Metrics

Our experiments are first conducted on the challenging public nuScenes [1] dataset, which contains 1000 driving scenes lasting 20 seconds respectively. Over 1.4M 3D bounding boxes of 23 categories are provided in total, which are annotated at 2Hz. Following the conventions [11, 17], Collision Rate (%) and L2 Displacement Error (DE) (m) are adopted to measure the open-loop planning performance. To study the effect of various perception encoders, we also evaluate the 3D object detection and online mapping results using mAP and NDS metrics respectively. Besides, Bench2Drive [15] provides a comprehensive benchmarking for evaluating multiple abilities of end-to-end AD systems in a closed-loop manner, which collects 1000 clips covering 44 interactive scenarios, 23 weathers and 12 towns in CARLA v2 [5]. Following the official settings, we use 950 clips for training while leaving 50 clips for open-loop evaluation. As for the closed-loop evaluation, we run the trained model in CARLA with 220 test routes and calculate the closed-loop metrics such as Driving Score (DS), Success Rate (SR) and Efficiency, respectively.

4.2. Implementation Details

DiFSD plans a $3s$ future ego-trajectory with $2s$ history information as input. Our DiFSD has two variants, namely DiFSD-S and DiFSD-B. As for DiFSD-S, both perspective-view perception version DiFSD-S (PV) and BEV perception version DiFSD-S (BEV) are all implemented for comparison. ResNet50 [8] is adopted as the default backbone network for visual encoding. The perception range is set to

$60m \times 30m$ longitudinally and laterally. Input image size of DiFSD-S is resized to 640×360 . For DiFSD-S (BEV), the default number of BEV query, map query, agent query is 100×100 , 100×20 and 300, respectively. For DiFSD-S (PV), N_{dec} is 6, N_a is 900 and N_m is 100 respectively. Each map element contains 20 map points. The feature dimension C is 256. The noise scale s is set to 2.0 and $0.2 \times FD$ for motion and planning respectively. G is set to 3. DiFSD-B has larger input image resolution (1280×720) and backbone network (ResNet101). We use AdamW [30] optimizer and Cosine Annealing [29] scheduler to train DiFSD with weight decay 0.01 and initial learning rate 2×10^{-4} . DiFSD is trained for 60 epochs and 4 epochs on nuScenes and Bench2Drive respectively, running on 8 NVIDIA Tesla A100 GPUs with batch size 8 empirically.

4.3. Main Results

Open-loop Planning Evaluation. As show in Tab. 1, DiFSD shows great advantages in both performance and efficiency compared with previous works. *On one hand, DiFSD-S achieves the minimum L2 error even with lightweight visual backbone and inferior BEV perception encoder.* Specifically, compared with BEVFormer-based end-to-end methods [11, 17], DiFSD-S (BEV) reduces the average L2 error by a great margin ($0.38m$ and $0.37m$, separately), while significantly reducing the average collision rates by 84% and 52% respectively. Equipped with deeper visual backbone and advanced sparse detectors from Perspective View (PV), the average L2 error and collision rates can be further reduced to $0.32m$ and to 0.06% respectively. *Notably, we are the first to achieve 0% collision rate on 1s.* On the other hand, benefiting from the ego-centric hierarchical interaction, *only sparse interactive agents (2%) are considered for motion planning.* Hence, DiFSD-S can achieve great efficiency with 14.8 FPS, $8.2 \times$ and $3.3 \times$ faster than UniAD [11] and VAD [17] respectively.

Closed-loop Planning Evaluation. We further validate the closed-loop performance in Bench2Drive [15], which has been proposed recently for comprehensive benchmarking of end-to-end planning methods. As shown in Tab. 2, AD-MLP [45] has a high L2 error and bad closed-loop planning performance using merely ego status as input, which is different from findings in nuScenes [1], demonstrating the behavior diversity in Bench2Drive. UniAD [11] has a lower L2 error compared to VAD [17] but with worse closed-loop planning performance as discussed in [21]. Notably, DiFSD-S achieves both the lowest L2 error and best closed-loop performance with great efficiency, showcasing the superiority and generalizability of our proposed method.

4.4. Ablation Study

We conduct extensive experiments to study the effectiveness of our DiFSD. We use DiFSD-S as default for ablation.

Table 1. Open-loop planning evaluation results on the nuScenes **val** dataset. * denotes multi-modality fusion method. † indicates evaluation with official checkpoint. ‡ indicates using evaluation protocol proposed in [21, 45].

Protocol	Method	Backbone	L2 (m) ↓				Collision (%) ↓				Latency (ms) ↓	FPS ↑
			1s	2s	3s	Avg.	1s	2s	3s	Avg.		
ST-P3 Metrics	ST-P3 [10]	EfficientNet-b4	1.33	2.11	2.90	2.11	0.23	0.62	1.27	0.71	628.3	1.6
	OccNet [37]	ResNet101-DCN	1.29	2.13	2.99	2.13	0.21	0.59	1.37	0.72	-	-
	FusionAD* [41]	ResNet101+SECOND [39]	-	-	-	1.03	0.25	0.13	0.25	0.21	-	-
	VAD-Base [17]	ResNet50	0.41	0.70	1.05	0.72	0.07	0.17	0.41	0.22	224.3	4.5
	SparseDrive-S [36]†	ResNet50	0.30	0.58	0.95	0.61	0.47	0.47	0.69	0.54	111.1	9.0
	DiFSD-S (BEV)	ResNet50	0.16	0.33	0.59	0.35	0.00	0.04	0.18	0.07	67.7	14.8
SparseDrive Metrics‡	UniAD [11]†	ResNet101-DCN	0.45	0.70	1.04	0.73	0.62	0.58	0.63	0.61	555.6	1.8
	VAD-Base [17]†	ResNet50	0.41	0.70	1.05	0.72	0.03	0.19	0.43	0.21	224.3	4.5
	SparseDrive-S [36]	ResNet50	0.29	0.58	0.96	0.61	0.01	0.05	0.18	0.08	111.1	9.0
	SparseDrive-B [36]	ResNet101	0.29	0.55	0.91	0.58	0.01	0.02	0.13	0.06	137.0	7.3
	DiFSD-S (BEV)	ResNet50	0.16	0.33	0.59	0.35	0.03	0.07	0.21	0.10	67.7	14.8
	DiFSD-S (PV)	ResNet50	0.15	0.31	0.56	0.33	0.00	0.06	0.19	0.08	93.7	10.7
	DiFSD-B (PV)	ResNet101	0.15	0.30	0.54	0.32	0.00	0.04	0.15	0.06	119.6	8.4

Table 2. Open-loop and Closed-loop planning evaluation results in Bench2Drive [15]. ResNet50 backbone is adopted for fair comparison. Avg. L2 is averaged over future 2 seconds under 2Hz.

Method	Open-loop Metric	Closed-loop Metrics		
	Avg. L2 ↓	DS ↑	SR ↑	Efficiency ↑
AD-MLP [45]	3.64	18.05	0.00	48.45
UniAD [11]	0.80	40.73	13.18	123.92
VAD [17]	0.91	42.35	15.00	157.94
DiFSD-S	0.70	52.02	21.00	178.30

More experiments are provided in the Appendix.

Necessity of Geometric Prior. We claim that the Closest In-Path Vehicle as well as Stationary (CIPV / CIPS) are more likely to interact with the ego-vehicle. To verify the necessity of such geometric prior, we conduct exhaustive ablations of the ego-centric query selector as show in Tab. 3. Without ego-centric selection, fewer objects randomly selected can result in worse planning results. While using the ego-centric cross attention, only 2% of surrounding queries are enough for achieving convincing planning performance. Besides, introducing the geometric prior through attention can dramatically reduce the L2 error and collision rate by 8% and 42% respectively. Meanwhile, when utilizing the ground-truth geometric score for upper-limit evaluation, we can obtain the extremely excellent planning performance (0.23m average L2 error). Undoubtedly, the proposed ego-centric query selector equipped with geometric attention is nontrivial for motion planner.

Effect of designs in Hierarchical Interaction. Tab. 4 shows the effectiveness of our elaborate designs in the hierarchical interaction module, which contains three main designs such as Dual Interaction (DI), Geometric Attention (GA) and Coarse-to-Fine Selection (CFS). DI models both ego-centric and object-centric interactions respectively, which improves the planning performance greatly as expected. GA facilitates the query selection process as

Table 3. Effect of ego-centric query selector and geometric prior.

Object Selection	Geometric Attention	Planning L2 (m) ↓				Planning Coll. (%) ↓			
		1s	2s	3s	Avg.	1s	2s	3s	Avg.
100%	✗	0.27	0.47	0.74	0.49	0.10	0.21	0.37	0.22
Random (5%)	✗	0.28	0.49	0.79	0.52	0.08	0.17	0.38	0.21
Random (2%)	✗	0.33	0.57	0.87	0.59	0.18	0.30	0.51	0.33
0%	✗	2.25	3.75	5.26	3.75	2.82	5.42	6.39	4.88
Attn (5%)	✗	0.16	0.34	0.63	0.38	0.07	0.09	0.31	0.16
Attn (2%)	✗	0.16	0.34	0.61	0.37	0.08	0.11	0.27	0.15
Attn (2%)	Random	0.17	0.36	0.67	0.40	0.07	0.10	0.34	0.17
Attn (2%)	GroundTruth	0.14	0.23	0.33	0.23	0.07	0.08	0.10	0.07
Attn (2%)	✓	0.16	0.33	0.59	0.35	0.00	0.04	0.18	0.07

Table 4. Ablation for designs in the hierarchical interaction. “DI” means dual interaction; “GA” means geometric attention; “CFS” means coarse-to-fine selection.

DI	GA	CFS	Planning L2 (m) ↓				Planning Coll. (%) ↓			
			1s	2s	3s	Avg.	1s	2s	3s	Avg.
✗	✓	✓	0.18	0.35	0.62	0.38	0.09	0.12	0.23	0.14
✓	✗	✓	0.16	0.34	0.61	0.37	0.08	0.11	0.27	0.15
✓	✓	✗	0.16	0.33	0.59	0.36	0.09	0.11	0.25	0.15
✓	✓	✓	0.16	0.33	0.59	0.35	0.00	0.04	0.18	0.07

discussed in Tab. 3, which reduces the collision rate by a great margin (42%). And CFS contributes to the interaction modeling quality through hierarchical receptive fields from global to local. All of these three designs combined together can achieve overall convincing planning performance.

Effect of designs in Motion Planner. As for motion planner in DiFSD, Joint Motion Prediction (JMP), Planning Optimization (PO) as well as Iterative Refinement (IR) makes up the planning pipeline of ego-vehicle. Besides, Uncertain Denoising (UD) contributes to the system stability and training convergence. Tab. 5 explores the effect of each design exhaustively. ID-1 indicates evaluating the proposal trajectory of ego-vehicle predicted together with interactive agents, which achieves competitive L2 error but is easier to collide with surrounding agents. ID-2 improves the collision rate greatly by 38.9% with the help of PO and planning

Table 5. Ablation for designs in the motion planner. “JMP” means joint motion prediction; “PO” means planning optimization; “IR” means iterative refinement. “UD” means uncertainty denoising.

ID	JMP	PO	IR	UD	Planning L2 (m) ↓				Planning Coll. (%) ↓			
					1s	2s	3s	Avg.	1s	2s	3s	Avg.
1	✓	✗	✗	✓	0.23	0.48	0.83	0.51	0.08	0.13	0.35	0.18
2	✓	✓	✗	✓	0.16	0.33	0.61	0.37	0.01	0.08	0.23	0.11
3	✓	✓	✓	✗	0.16	0.34	0.64	0.38	0.07	0.07	0.17	0.10
4	✓	✓	✓	✓	0.16	0.33	0.59	0.35	0.00	0.04	0.18	0.07

Table 6. Ablation for number of iterative refinement stages.

Number of stages	Planning L2 (m) ↓				Planning Coll. (%) ↓			
	1s	2s	3s	Avg.	1s	2s	3s	Avg.
1	0.16	0.33	0.61	0.37	0.01	0.08	0.23	0.11
2	0.16	0.33	0.59	0.35	0.00	0.04	0.18	0.07
3	0.16	0.33	0.60	0.36	0.01	0.40	0.22	0.09
4	0.16	0.33	0.61	0.36	0.00	0.04	0.20	0.08

constraints [17] during training phase. ID-4 emphasizes the importance of IR in improving the quality of ego-planning trajectory (average 5.4% L2 error and 36.3% collision rate reduction respectively). ID-3 reflects the benefit of UD used for end-to-end training compared to ID-4.

Effect of Iterative Refinement stages. We continue to study the number of refinement stages in Tab. 6. We can observe that our DiFSD can obtain superior planning performance with one additional refinement stage (36.3% collision rate reduction), which becomes saturated when introducing more stages. Hence, two-stage interacted motion planner is enough for achieving convincing results.

Effect of Uncertainty Denoising. We also validate the effectiveness of uncertainty denoising strategy including position-level motion diffusion and trajectory-level planning denoising. As shown in Tab. 7, motion diffusion can improve the prediction stability with uncertain agent positions, while the planning denoising can also strengthen the trajectory regression precision of ego-vehicle.

Runtime of each module. We evaluate the modular runtime of DiFSD-S with different perception paradigms as shown in Tab. 8. Generally, visual backbone and perception encoder occupy the most of the runtime for feature extraction and scene understanding. Hierarchical interaction also takes a significant part for interaction modeling and interactive query selection. Thanks to the ego-centric interaction and selection module, the joint motion planner only consumes 7.9ms to plan the future ego-trajectory. *Notably, though PV-based perception module [24] achieves superior detection performance, it consumes more computation cost due to the repeated query projection, deformable feature aggregation as well as the symmetric sparse perception architecture for unified object detection and on-line mapping, without a shared BEV feature as [11, 17].*

4.5. Qualitative Results

We visualize the motion trajectories of sparse interactive agents as well as planning results of DiFSD as illustrated

Table 7. Ablation for uncertainty denoising procedure.

Position Diffusion	Trajectory Denoising	Planning L2 (m) ↓				Planning Coll. (%) ↓			
		1s	2s	3s	Avg.	1s	2s	3s	Avg.
✗	✗	0.16	0.34	0.64	0.38	0.07	0.07	0.17	0.10
✓	✗	0.16	0.34	0.63	0.37	0.02	0.04	0.15	0.07
✓	✓	0.16	0.33	0.59	0.35	0.00	0.04	0.18	0.07

Table 8. Module runtime statistics. The inference speed is measured for DiFSD-S on one NVIDIA Tesla A100 GPU.

Module	Bird’s-Eye View (BEV) Perception		Perspective-View (PV) Perception	
	Latency (ms)	Proportion (%)	Latency (ms)	Proportion (%)
Backbone	8.4	12.4	11.0	11.8
Perception Encoder	34.4	50.8	54.9	58.6
Hierarchical Interaction	17.0	25.1	19.9	21.2
Motion Prediction	4.5	6.6	4.5	4.8
Planning Optimization	3.4	5.1	3.4	3.6
Total	67.7	100	93.7	100

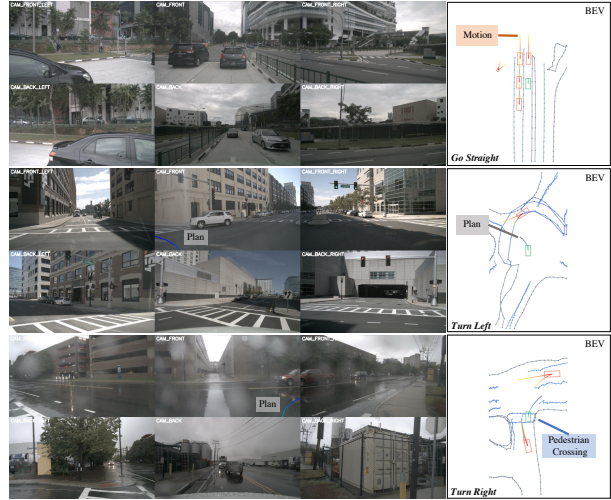


Figure 5. Qualitative results of DiFSD. DiFSD outputs planning results based on hierarchical interaction and joint motion of sparse interactive agents without considering other irrelevant objects. We omit the map selection results for clarity of road structure details.

in Fig. 5. Both surrounding camera images and prediction results on BEV are provided accordingly. Besides, we also project the planning trajectories to the front-view camera image. Only the top-3 trajectories of selected agents interacting with ego-vehicle are visualized for better understanding of DiFSD motivation. DiFSD outputs planning results based on the vectorized representation in an end-to-end manner, not requiring any dense interaction and redundant motion modeling, let alone hand-crafted post-processing.

5. Conclusion

In this paper, we propose a fully sparse paradigm for end-to-end self-driving in an ego-centric manner, termed as DiFSD. DiFSD revisits the human driving behavior and conducts hierarchical interaction based on sparse representation and perception results. Only interactive agents are considered for joint motion prediction with the ego-vehicle. Iterative planning optimization strategy contributes to the driving safety with high efficiency. Besides, uncertainty

modeling is conducted to improve the stability of end-to-end system. Extensive ablations and comparisons reveal the superiority and great potential of our ego-centric fully sparse paradigm for future research.

References

- [1] Holger Caesar, Varun Bankiti, Alex H Lang, Sourabh Vora, Venice Erin Liong, Qiang Xu, Anush Krishnan, Yu Pan, Giancarlo Baldan, and Oscar Beijbom. nuscnets: A multi-modal dataset for autonomous driving. In *Proceedings of the IEEE Conference on Computer Vision and Pattern Recognition*, pages 11621–11631, 2020. [2](#), [6](#), [1](#)
- [2] Sergio Casas, Wenjie Luo, and Raquel Urtasun. Intentnet: Learning to predict intention from raw sensor data. In *Conference on Robot Learning*, pages 947–956. PMLR, 2018. [2](#)
- [3] Felipe Codevilla, Matthias Müller, Antonio López, Vladlen Koltun, and Alexey Dosovitskiy. End-to-end driving via conditional imitation learning. In *2018 IEEE International Conference on Robotics and Automation*, pages 4693–4700. IEEE, 2018. [3](#)
- [4] Felipe Codevilla, Eder Santana, Antonio M López, and Adrien Gaidon. Exploring the limitations of behavior cloning for autonomous driving. In *Proceedings of the IEEE International Conference on Computer Vision*, pages 9329–9338, 2019. [3](#)
- [5] Alexey Dosovitskiy, German Ros, Felipe Codevilla, Antonio Lopez, and Vladlen Koltun. Carla: An open urban driving simulator. In *Conference on Robot Learning*, pages 1–16. PMLR, 2017. [6](#)
- [6] Junru Gu, Chenxu Hu, Tianyuan Zhang, Xuanyao Chen, Yilun Wang, Yue Wang, and Hang Zhao. Vip3d: End-to-end visual trajectory prediction via 3d agent queries. In *Proceedings of the IEEE Conference on Computer Vision and Pattern Recognition*, pages 5496–5506, 2023. [3](#)
- [7] Chunrui Han, Jinrong Yang, Jianjian Sun, Zheng Ge, Runpei Dong, Hongyu Zhou, Weixin Mao, Yuang Peng, and Xiangyu Zhang. Exploring recurrent long-term temporal fusion for multi-view 3d perception. *IEEE Robotics and Automation Letters*, 2024. [2](#)
- [8] Kaiming He, Xiangyu Zhang, Shaoqing Ren, and Jian Sun. Deep residual learning for image recognition. In *Proceedings of the IEEE Conference on Computer Vision and Pattern Recognition*, pages 770–778, 2016. [3](#), [6](#)
- [9] Jie Hu, Li Shen, and Gang Sun. Squeeze-and-excitation networks. In *Proceedings of the IEEE Conference on Computer Vision and Pattern Recognition*, pages 7132–7141, 2018. [4](#)
- [10] Shengchao Hu, Li Chen, Penghao Wu, Hongyang Li, Junchi Yan, and Dacheng Tao. St-p3: End-to-end vision-based autonomous driving via spatial-temporal feature learning. In *European Conference on Computer Vision*, pages 533–549. Springer, 2022. [7](#)
- [11] Yihan Hu, Jiazhi Yang, Li Chen, Keyu Li, Chonghao Sima, Xizhou Zhu, Siqi Chai, Senyao Du, Tianwei Lin, Wenhai Wang, et al. Planning-oriented autonomous driving. In *Proceedings of the IEEE Conference on Computer Vision and Pattern Recognition*, pages 17853–17862, 2023. [1](#), [2](#), [3](#), [5](#), [6](#), [7](#), [8](#)
- [12] Bin Huang, Yangguang Li, Enze Xie, Feng Liang, Luya Wang, Mingzhu Shen, Fenggang Liu, Tianqi Wang, Ping Luo, and Jing Shao. Fast-bev: Towards real-time on-vehicle bird’s-eye view perception. *arXiv preprint arXiv:2301.07870*, 2023. [2](#)
- [13] Junjie Huang and Guan Huang. Bevdet4d: Exploit temporal cues in multi-camera 3d object detection. *arXiv preprint arXiv:2203.17054*, 2022. [2](#)
- [14] Junjie Huang, Guan Huang, Zheng Zhu, Yun Ye, and Dalong Du. Bevdet: High-performance multi-camera 3d object detection in bird-eye-view. *arXiv preprint arXiv:2112.11790*, 2021. [2](#)
- [15] Xiaosong Jia, Zhenjie Yang, Qifeng Li, Zhiyuan Zhang, and Junchi Yan. Bench2drive: Towards multi-ability benchmarking of closed-loop end-to-end autonomous driving. *arXiv preprint arXiv:2406.03877*, 2024. [2](#), [6](#), [7](#)
- [16] Bo Jiang, Shaoyu Chen, Xinggang Wang, Bencheng Liao, Tianheng Cheng, Jiajie Chen, Helong Zhou, Qian Zhang, Wenyu Liu, and Chang Huang. Perceive, interact, predict: Learning dynamic and static clues for end-to-end motion prediction. *arXiv preprint arXiv:2212.02181*, 2022. [3](#)
- [17] Bo Jiang, Shaoyu Chen, Qing Xu, Bencheng Liao, Jiajie Chen, Helong Zhou, Qian Zhang, Wenyu Liu, Chang Huang, and Xinggang Wang. Vad: Vectorized scene representation for efficient autonomous driving. In *Proceedings of the IEEE International Conference on Computer Vision*, pages 8340–8350, 2023. [1](#), [2](#), [3](#), [5](#), [6](#), [7](#), [8](#)
- [18] Qi Li, Yue Wang, Yilun Wang, and Hang Zhao. Hdmmapnet: An online hd map construction and evaluation framework. In *2022 International Conference on Robotics and Automation*, pages 4628–4634. IEEE, 2022. [2](#)
- [19] Yinhao Li, Zheng Ge, Guanyi Yu, Jinrong Yang, Zengran Wang, Yukang Shi, Jianjian Sun, and Zeming Li. Bevdepth: Acquisition of reliable depth for multi-view 3d object detection. In *Proceedings of the AAAI Conference on Artificial Intelligence*, pages 1477–1485, 2023. [2](#)
- [20] Zhiqi Li, Wenhai Wang, Hongyang Li, Enze Xie, Chonghao Sima, Tong Lu, Yu Qiao, and Jifeng Dai. Bevformer: Learning bird’s-eye-view representation from multi-camera images via spatiotemporal transformers. In *European Conference on Computer Vision*, pages 1–18. Springer, 2022. [2](#), [1](#)
- [21] Zhiqi Li, Zhiding Yu, Shiyi Lan, Jiahao Li, Jan Kautz, Tong Lu, and Jose M Alvarez. Is ego status all you need for open-loop end-to-end autonomous driving? In *Proceedings of the IEEE Conference on Computer Vision and Pattern Recognition*, pages 14864–14873, 2024. [6](#), [7](#), [1](#)
- [22] Ming Liang, Bin Yang, Wenyuan Zeng, Yun Chen, Rui Hu, Sergio Casas, and Raquel Urtasun. Pnpnet: End-to-end perception and prediction with tracking in the loop. In *Proceedings of the IEEE Conference on Computer Vision and Pattern Recognition*, pages 11553–11562, 2020. [2](#)
- [23] Bencheng Liao, Shaoyu Chen, Xinggang Wang, Tianheng Cheng, Qian Zhang, Wenyu Liu, and Chang Huang. Maptr: Structured modeling and learning for online vectorized hd

- map construction. *arXiv preprint arXiv:2208.14437*, 2022. [2](#)
- [24] Xuewu Lin, Zixiang Pei, Tianwei Lin, Lichao Huang, and Zhizhong Su. Sparse4d v3: Advancing end-to-end 3d detection and tracking. *arXiv preprint arXiv:2311.11722*, 2023. [2](#), [3](#), [8](#), [1](#)
- [25] Haisong Liu, Yao Teng, Tao Lu, Haiguang Wang, and Limin Wang. Sparsebev: High-performance sparse 3d object detection from multi-camera videos. In *Proceedings of the IEEE International Conference on Computer Vision*, pages 18580–18590, 2023. [3](#)
- [26] Yingfei Liu, Tiancai Wang, Xiangyu Zhang, and Jian Sun. Petr: Position embedding transformation for multi-view 3d object detection. In *European Conference on Computer Vision*, pages 531–548. Springer, 2022.
- [27] Yingfei Liu, Junjie Yan, Fan Jia, Shuailin Li, Aqi Gao, Tiancai Wang, and Xiangyu Zhang. Petrv2: A unified framework for 3d perception from multi-camera images. In *Proceedings of the IEEE International Conference on Computer Vision*, pages 3262–3272, 2023. [2](#)
- [28] Yicheng Liu, Tianyuan Yuan, Yue Wang, Yilun Wang, and Hang Zhao. Vectormapnet: End-to-end vectorized hd map learning. In *International Conference on Machine Learning*, pages 22352–22369. PMLR, 2023. [2](#)
- [29] Ilya Loshchilov and Frank Hutter. Sgdr: Stochastic gradient descent with warm restarts. *arXiv preprint arXiv:1608.03983*, 2016. [6](#)
- [30] Ilya Loshchilov and Frank Hutter. Decoupled weight decay regularization. *arXiv preprint arXiv:1711.05101*, 2017. [6](#)
- [31] Wenjie Luo, Bin Yang, and Raquel Urtasun. Fast and furious: Real time end-to-end 3d detection, tracking and motion forecasting with a single convolutional net. In *Proceedings of the IEEE Conference on Computer Vision and Pattern Recognition*, pages 3569–3577, 2018. [2](#)
- [32] Tim Meinhardt, Alexander Kirillov, Laura Leal-Taixe, and Christoph Feichtenhofer. Trackformer: Multi-object tracking with transformers. In *Proceedings of the IEEE Conference on Computer Vision and Pattern Recognition*, pages 8844–8854, 2022. [2](#)
- [33] Jonah Philion and Sanja Fidler. Lift, splat, shoot: Encoding images from arbitrary camera rigs by implicitly unprojecting to 3d. In *Computer Vision—ECCV 2020: 16th European Conference, Glasgow, UK, August 23–28, 2020, Proceedings, Part XIV 16*, pages 194–210. Springer, 2020. [2](#)
- [34] Aditya Prakash, Kashyap Chitta, and Andreas Geiger. Multi-modal fusion transformer for end-to-end autonomous driving. In *Proceedings of the IEEE Conference on Computer Vision and Pattern Recognition*, pages 7077–7087, 2021. [3](#)
- [35] Peize Sun, J Cao, Y Jiang, R Zhang, E Xie, Z Yuan, C Wang, and P Luo. Transtrack: Multiple object tracking with transformer. arxiv 2020. *arXiv preprint arXiv:2012.15460*, 2012. [2](#)
- [36] Wenchao Sun, Xuewu Lin, Yining Shi, Chuang Zhang, Hao-ran Wu, and Sifa Zheng. Sparsedrive: End-to-end autonomous driving via sparse scene representation. *arXiv preprint arXiv:2405.19620*, 2024. [1](#), [3](#), [7](#), [2](#)
- [37] Wenwen Tong, Chonghao Sima, Tai Wang, Li Chen, Silei Wu, Hanming Deng, Yi Gu, Lewei Lu, Ping Luo, Dahua Lin, et al. Scene as occupancy. In *Proceedings of the IEEE International Conference on Computer Vision*, pages 8406–8415, 2023. [7](#)
- [38] Yue Wang, Vitor Campagnolo Guizilini, Tianyuan Zhang, Yilun Wang, Hang Zhao, and Justin Solomon. Detr3d: 3d object detection from multi-view images via 3d-to-2d queries. In *Conference on Robot Learning*, pages 180–191. PMLR, 2022. [2](#)
- [39] Yan Yan, Yuxing Mao, and Bo Li. Second: Sparsely embedded convolutional detection. *Sensors*, 18(10):3337, 2018. [7](#)
- [40] Chenyu Yang, Yuntao Chen, Hao Tian, Chenxin Tao, Xizhou Zhu, Zhaoxiang Zhang, Gao Huang, Hongyang Li, Yu Qiao, Lewei Lu, et al. Bevformer v2: Adapting modern image backbones to bird’s-eye-view recognition via perspective supervision. In *Proceedings of the IEEE Conference on Computer Vision and Pattern Recognition*, pages 17830–17839, 2023. [2](#)
- [41] Tengju Ye, Wei Jing, Chunyong Hu, Shikun Huang, Lingping Gao, Fangzhen Li, Jingke Wang, Ke Guo, Wencong Xiao, Weibo Mao, et al. Fusionad: Multi-modality fusion for prediction and planning tasks of autonomous driving. *arXiv preprint arXiv:2308.01006*, 2023. [1](#), [3](#), [5](#), [6](#), [7](#)
- [42] En Yu, Tiancai Wang, Zhuoling Li, Yuang Zhang, Xiangyu Zhang, and Wenbing Tao. Motrv3: Release-fetch supervision for end-to-end multi-object tracking. *arXiv preprint arXiv:2305.14298*, 2023. [2](#)
- [43] Tianyuan Yuan, Yicheng Liu, Yue Wang, Yilun Wang, and Hang Zhao. Streammapnet: Streaming mapping network for vectorized online hd map construction. In *Proceedings of the IEEE Winter Conference on Applications of Computer Vision*, pages 7356–7365, 2024. [2](#)
- [44] Fangao Zeng, Bin Dong, Yuang Zhang, Tiancai Wang, Xiangyu Zhang, and Yichen Wei. Motr: End-to-end multiple-object tracking with transformer. In *European Conference on Computer Vision*, pages 659–675. Springer, 2022. [2](#)
- [45] Jiang-Tian Zhai, Ze Feng, Jinhao Du, Yongqiang Mao, Jiang-Jiang Liu, Zichang Tan, Yifu Zhang, Xiaoqing Ye, and Jingdong Wang. Rethinking the open-loop evaluation of end-to-end autonomous driving in nuscenec. *arXiv preprint arXiv:2305.10430*, 2023. [6](#), [7](#), [1](#)
- [46] Yuang Zhang, Tiancai Wang, and Xiangyu Zhang. Motrv2: Bootstrapping end-to-end multi-object tracking by pre-trained object detectors. In *Proceedings of the IEEE Conference on Computer Vision and Pattern Recognition*, pages 22056–22065, 2023. [2](#)
- [47] Yunpeng Zhang, Deheng Qian, Ding Li, Yifeng Pan, Yong Chen, Zhenbao Liang, Zhiyao Zhang, Shurui Zhang, Hongxu Li, Maolei Fu, et al. Graphad: Interaction scene graph for end-to-end autonomous driving. *arXiv preprint arXiv:2403.19098*, 2024. [3](#)



DiFSD: Ego-Centric Fully Sparse Paradigm with Uncertainty Denoising and Iterative Refinement for Efficient End-to-End Self-Driving

Supplementary Material

A. Evaluation Metrics

Perception. The evaluation for detection and tracking follows standard evaluation protocols [1]. For detection, we use mean Average Precision(mAP), mean Average Error of Translation(mATE), Scale(mASE), Orientation(mAOE), Velocity(mAVE), Attribute(mAAE) and nuScenes Detection Score(NDS) to evaluate the model performance. For online mapping, we calculate the Average Precision(AP) of three map classes: lane divider, pedestrian crossing and road boundary, then average across all classes to get mean Average Precision (mAP).

Planning. We adopt commonly used L2 error and collision rate to evaluate the planning performance. The evaluation of L2 error is aligned with VAD [17]. For collision rate, there are two drawbacks in previous [11, 17] implementation, resulting in inaccurate evaluation in planning performance. On one hand, previous benchmark convert obstacle bounding boxes into occupancy map with a grid size of 0.5m, resulting in false collisions in certain cases, e.g. ego vehicle approaches obstacles that smaller than a single occupancy map pixel [45]. (2) The heading of ego vehicle is not considered and assumed to remain unchanged [21]. To accurately evaluate the planning performance, we account for the changes in ego heading by estimating the yaw angle through trajectory points, and assess the presence of a collision by examining the overlap between the bounding boxes of ego vehicle and obstacles. We reproduce the planning results on our benchmark with official checkpoints [11, 17] for a fair comparison.

B. More Ablation Study

Necessity and Order of Object Selection. Tab. 1 studies the necessity of agent and map selection during the ego-centric hierarchical interaction. We can observe that agent selection contributes more than the map selection, especially in the driving safety. And both of agent and map interactions are conducted in a cascaded order is inferior than the parallel manner, where the updated ego query from parallel outputs are concatenated for joint motion prediction.

Effect of Interactive Score Fusion. During the ego-centric query selection, both geometric and classification scores are considered to ensure that the selected closest in-path queries are true positive agents or maps, which are adopted for motion planner. Tab. 2 shows the effect of three types of scores used for query ranking, namely attention, geometry

Table 1. Necessity of agent and map selection as well as effect of interaction order in the hierarchical interaction module.

Agent Selection	Map Selection	Cascade	Parallel	Planning L2 (m) ↓				Planning Coll. (%) ↓			
				1s	2s	3s	Avg.	1s	2s	3s	Avg.
✓	✗	-	-	0.16	0.34	0.64	0.38	0.03	0.05	0.22	0.10
✗	✓	-	-	0.17	0.35	0.63	0.38	0.02	0.06	0.28	0.12
✓	✓	✓	-	0.16	0.34	0.62	0.37	0.05	0.07	0.30	0.14
✓	✓	-	✓	0.16	0.33	0.59	0.35	0.00	0.04	0.18	0.07

Table 2. Effect of interactive score fusion process in the geometric attended selection step.

Attention Score	Geometric Score	Classification Score	Planning L2 (m) ↓				Planning Coll. (%) ↓			
			1s	2s	3s	Avg.	1s	2s	3s	Avg.
✓	✗	✗	0.18	0.36	0.66	0.39	0.09	0.11	0.28	0.16
✓	✓	✗	0.17	0.35	0.65	0.38	0.01	0.07	0.24	0.11
✓	✓	✓	0.16	0.33	0.59	0.35	0.00	0.04	0.18	0.07

and confidence scores. As Eq. 1, interactive score S_{inter} obtained by multiplying these three scores can achieve the best selection quality and planning performance. S_{inter} without confidence score fails to distinguish between background and foreground queries, resulting in inferior performance.

Effect of Sparse Perception. Recent end-to-end planning method [36] resorts to the sparse perception fashion to provide advanced 3D detection and online mapping results with high efficiency. To study the significance of advanced perception encoders for ego-planning, we compare the perception performance of various end-to-end methods as shown in Tab. 3. With sparse perception encoder [24], the performance of 3D object detection and online mapping can be greatly improved (10.6 NDS and 7.5 mAP, respectively) compared with dense BEV-based perception paradigm [20]. And the end-to-end planner [36] equipped with the advanced perception encoder can consistently boost the planning performance. Therefore, the perception performance is essential for the end-to-end planner.

C. Analysis & Discussion

The GroundTruth future state distribution of ego-vehicle on nuScenes validation set is illustrated in Fig. A1, which is calculated with fixed time interval (1s) between consecutive predicted waypoints. And we also compare the output ego-state distribution of different popular end-to-end methods based on planned trajectories respectively, as show in Fig. A2. We can observe that without ego-centric design, the optimized end-to-end model is unable to handle various emergencies appearing in the driving scenarios, where the absolute values of Δv and Δa are larger than normal

Table 3. Comparison of perception results (3D detection and online mapping) of state-of-the-art perception or end-to-end methods on nuScenes **val** dataset. †: Reproduced with official checkpoint. * indicates to use pre-trained weights from the nuImage dataset.

Method	Backbone	BEV	mAP \uparrow	NDS \uparrow
BEVFormer [20]	ResNet101-DCN	✓	41.6	51.7
Sparse4Dv3 [24]	ResNet101*	✗	53.7	62.3
UniAD [11]	ResNet101-DCN	✓	38.0	49.8
VAD† [17]	ResNet50	✓	27.3	39.7
SparseDrive-S [36]	ResNet50	✗	41.8	52.5
SparseDrive-B [36]	ResNet101*	✗	49.6	58.8
DiFSD-S	ResNet50	✓	32.8	45.8
DiFSD-S	ResNet50	✗	41.0	52.8
DiFSD-B	ResNet101*	✗	49.6	58.9

(a) 3D detection results.

Method	AP _{ped} \uparrow	AP _{divider} \uparrow	AP _{boundary} \uparrow	mAP \uparrow
VectorMapNet [28]	36.1	47.3	39.3	40.9
MapTR [23]	56.2	59.8	60.1	58.7
VAD† [17]	40.6	51.5	50.6	47.6
SparseDrive-S [36]	49.9	57.0	58.4	55.1
SparseDrive-B [36]	53.2	56.3	59.1	56.2
DiFSD-S (BEV)	46.7	54.3	56.0	52.3
DiFSD-S (PV)	54.9	55.7	57.3	56.0
DiFSD-B (PV)	52.3	58.2	59.3	56.6

(b) Online mapping results

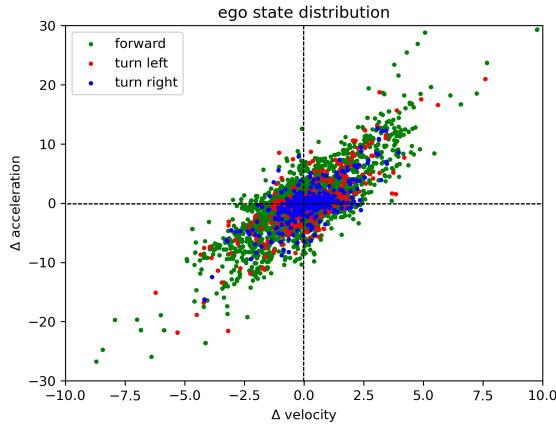


Figure A1. Distribution of GroundTruth future ego states (Δv vs. Δa) with different driving commands on the nuScenes **val** set.

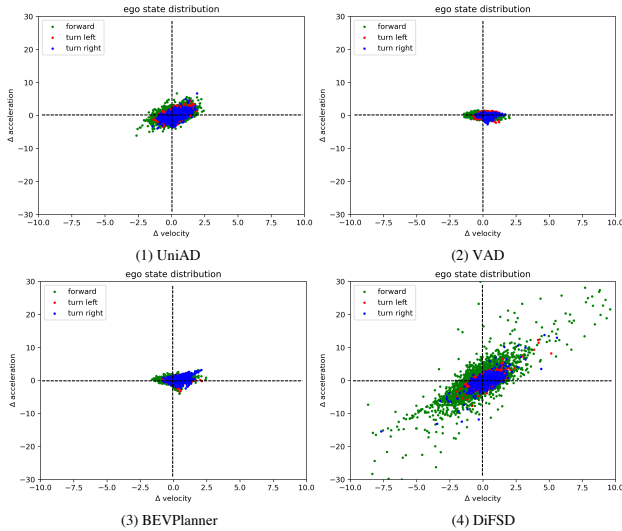


Figure A2. Comparison of predicted future ego states of different end-to-end methods on the validation set of nuScenes.

situations. Under this circumstance, the output planned trajectories cannot conform to the expert routes as expected. However, our DiFSD performs consistently better in planning the future ego states with variable speed and acceleration, owing to the ego-centric hierarchical interaction and selection mechanism, thus the iterative motion planner can focus on the interactive agents rather than irrelevant objects.

D. Visualization

As show in Fig. A3-A5, we provide more visualization results to illustrate the effectiveness of DiFSD on various driving scenarios (*i.e.*, interactive / non-interactive scenes, lane-change / lane-keep / following scenes, overtaking / avoidance scenes, intersection scenes) under different commands (*i.e.*, “Go Straight”, “Turn Left”, “Turn Right”).

Moreover, we also observe some failure cases on nuScenes validation set as illustrated in Fig. A6 and Fig. A7. The corresponding explanations as well as analysis are described in the captions below respectively, which mainly attribute to the irrationality of the expert (ground truth) future trajectories of ego vehicle, demonstrating the strong generalizability of our proposed DiFSD in planning the efficient and reasonable results based on the selected sparse representations of surrounding driving scenarios.



Figure A3. Qualitative results of DiFSD under “Go Straight” driving command in interactive scenes. In the first row, the pedestrian and the construction vehicle are selected as the closest in-path agents for motion prediction and interactive planning, thus DiFSD adjusts the planned trajectory from afar to avoid a collision. In the second row, DiFSD notices the pedestrian in the distance and plans the future trajectory taking the pedestrian intention into consideration. In the third row, DiFSD completes interactive decision-making in the “Cut-in” scenario, and outputs the planned trajectory constrained by the lane divider.

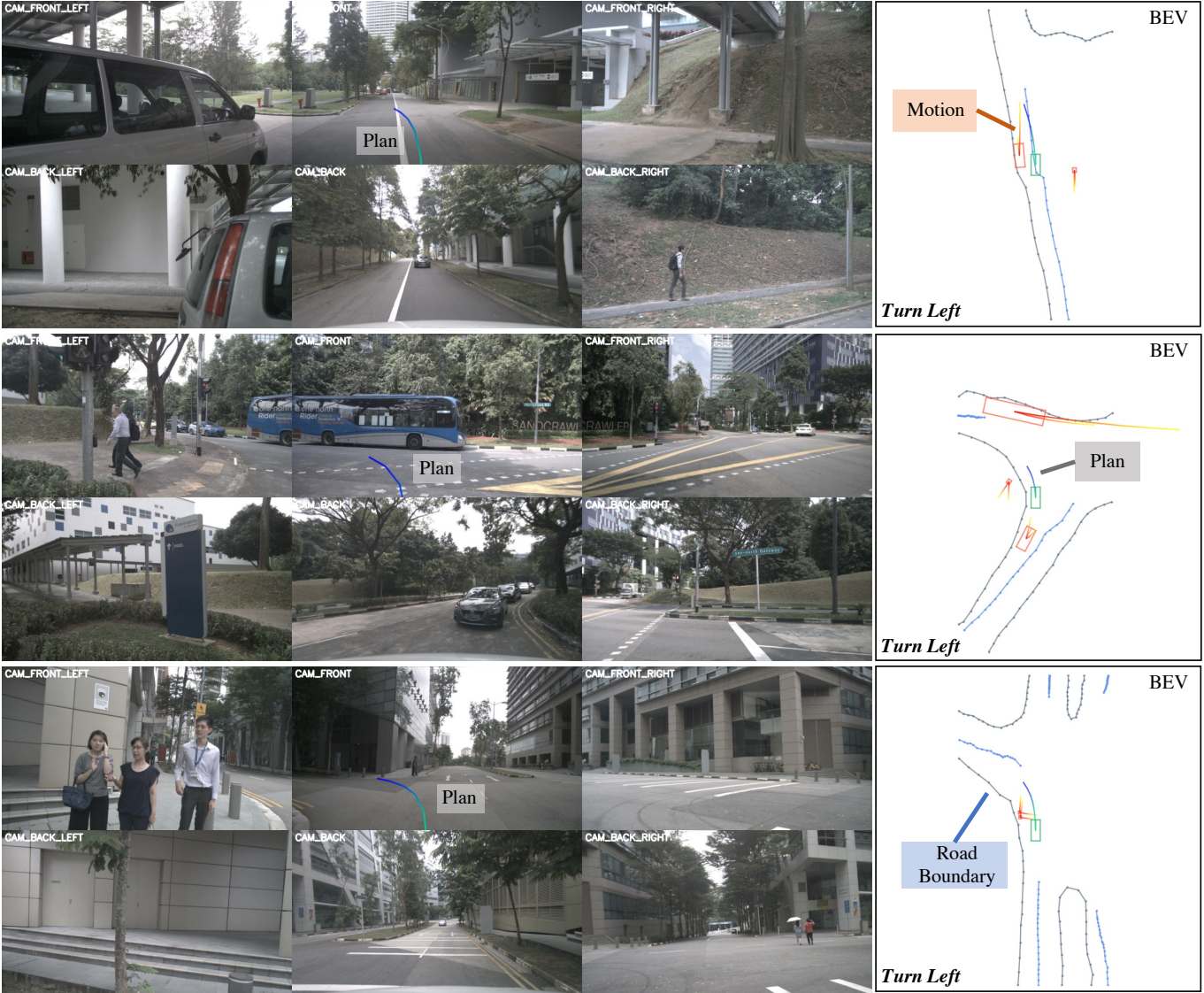


Figure A4. Qualitative results of DiFSD under “Turn Left” driving command in diverse scenarios. In the first scenario, DiFSD makes an “Overtaking” decision from the ride side of the front vehicle, considering the motions of both target vehicle and neighboring pedestrian to ensure driving safety. In the latter two intersection scenarios, DiFSD detects the pedestrians waiting at the crossing and the opposite bus passing the intersection, then decelerates to make a turning decision.

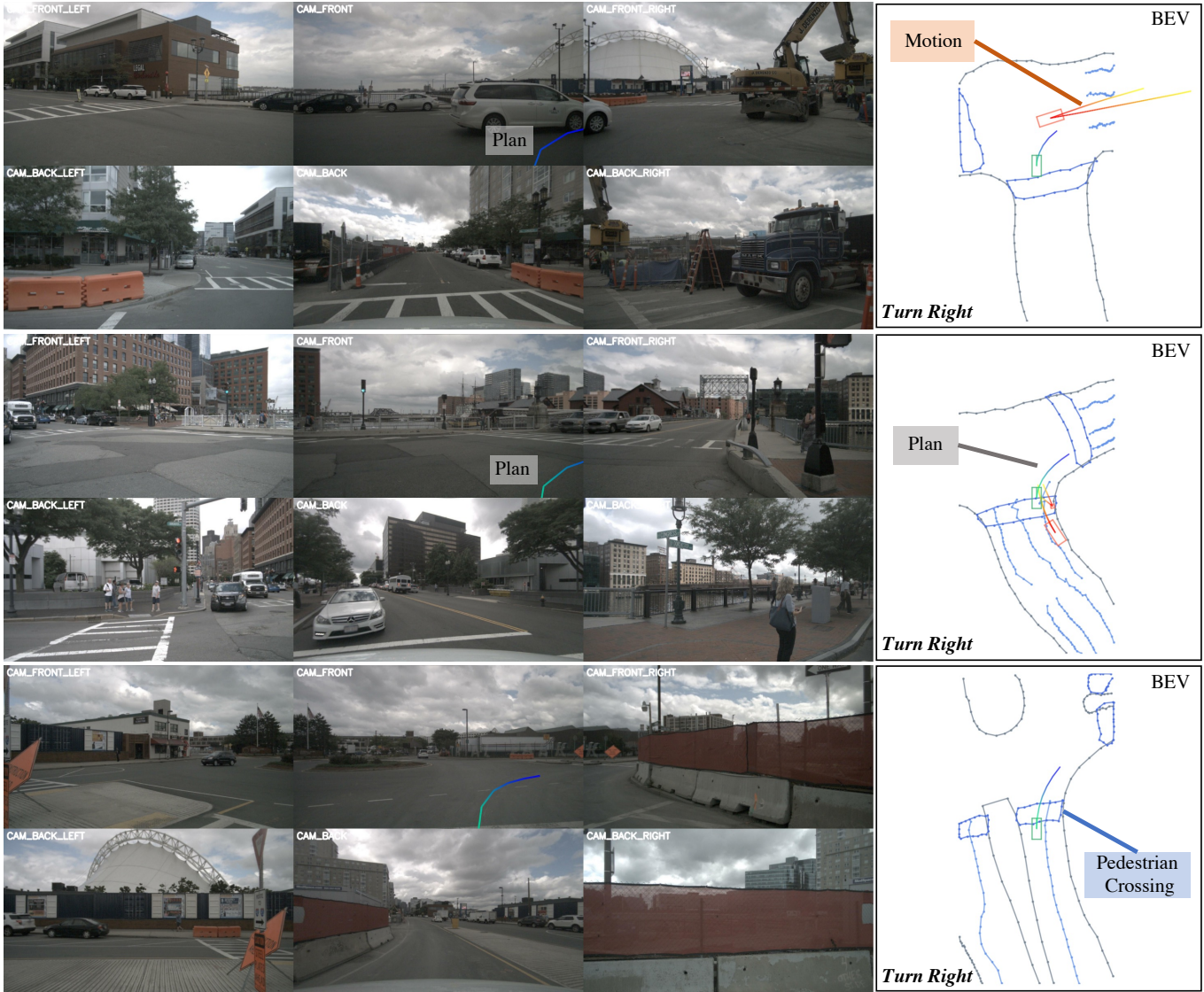


Figure A5. Qualitative results of DiFSD under “Turn Right” driving command at both interactive and non-interactive intersections. Joint motion prediction of agents and ego-vehicle is essential for DiFSD especially in the turning scenarios at interactions. The first two rows illustrate the interactive scenarios either inside and outside the intersection. And the last row presents a non-interactive intersection where DiFSD plans the future trajectory merely based on the detected pedestrian crossing.

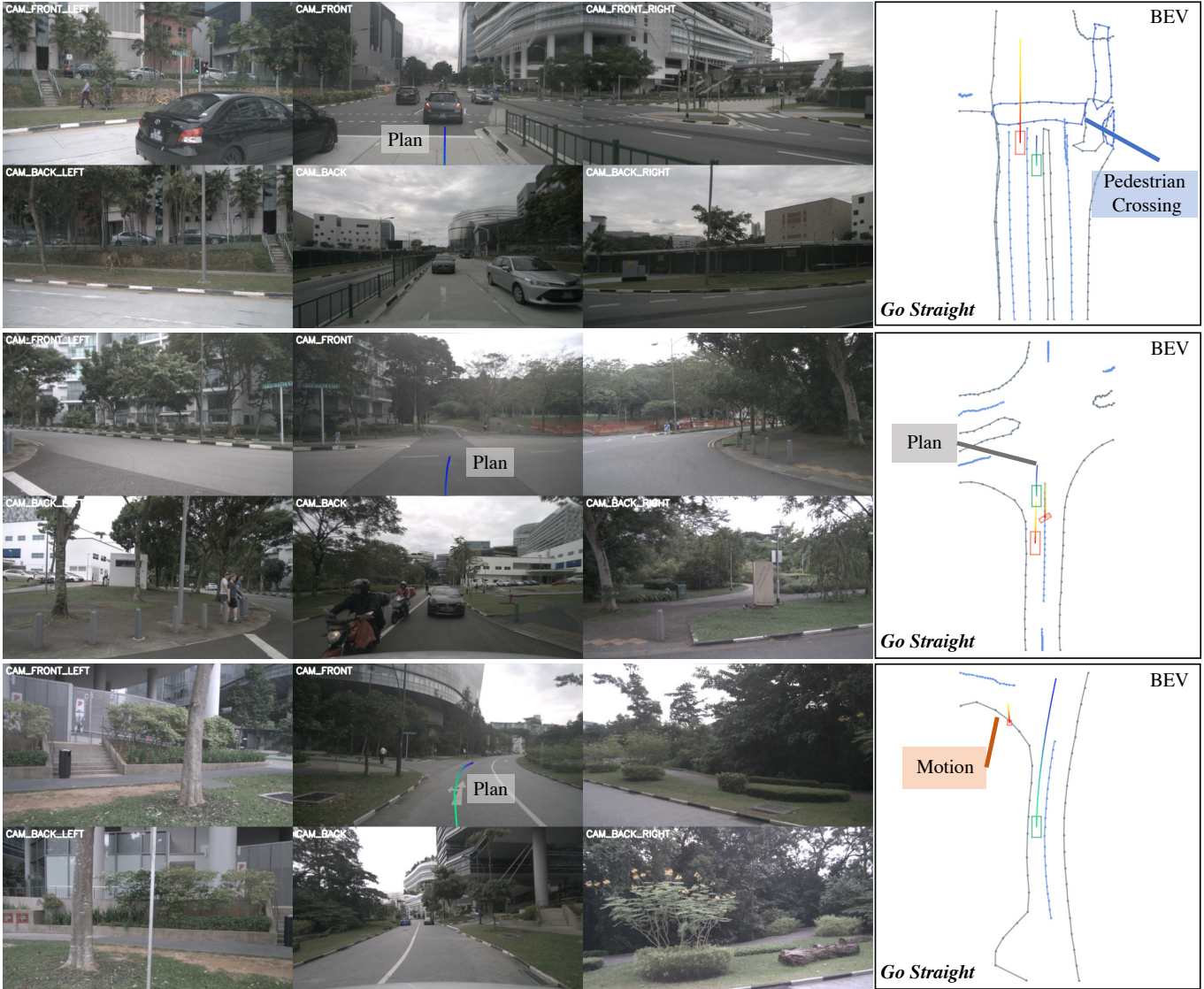


Figure A6. Failure cases of DiFSD with stationary status. The ego-vehicle is found to remain stationary in either crowded “car-following” or spacious “intersection-crossing” scenarios, while DiFSD still outputs a straight-ahead planning result. However, from the selected perception and motion results, moving forward in these scenarios is also an alternative choice and more reasonable. This also indicates our DiFSD doesn’t depend on the previous ego status during the planning stage, without introducing the motion priors of ego vehicle.

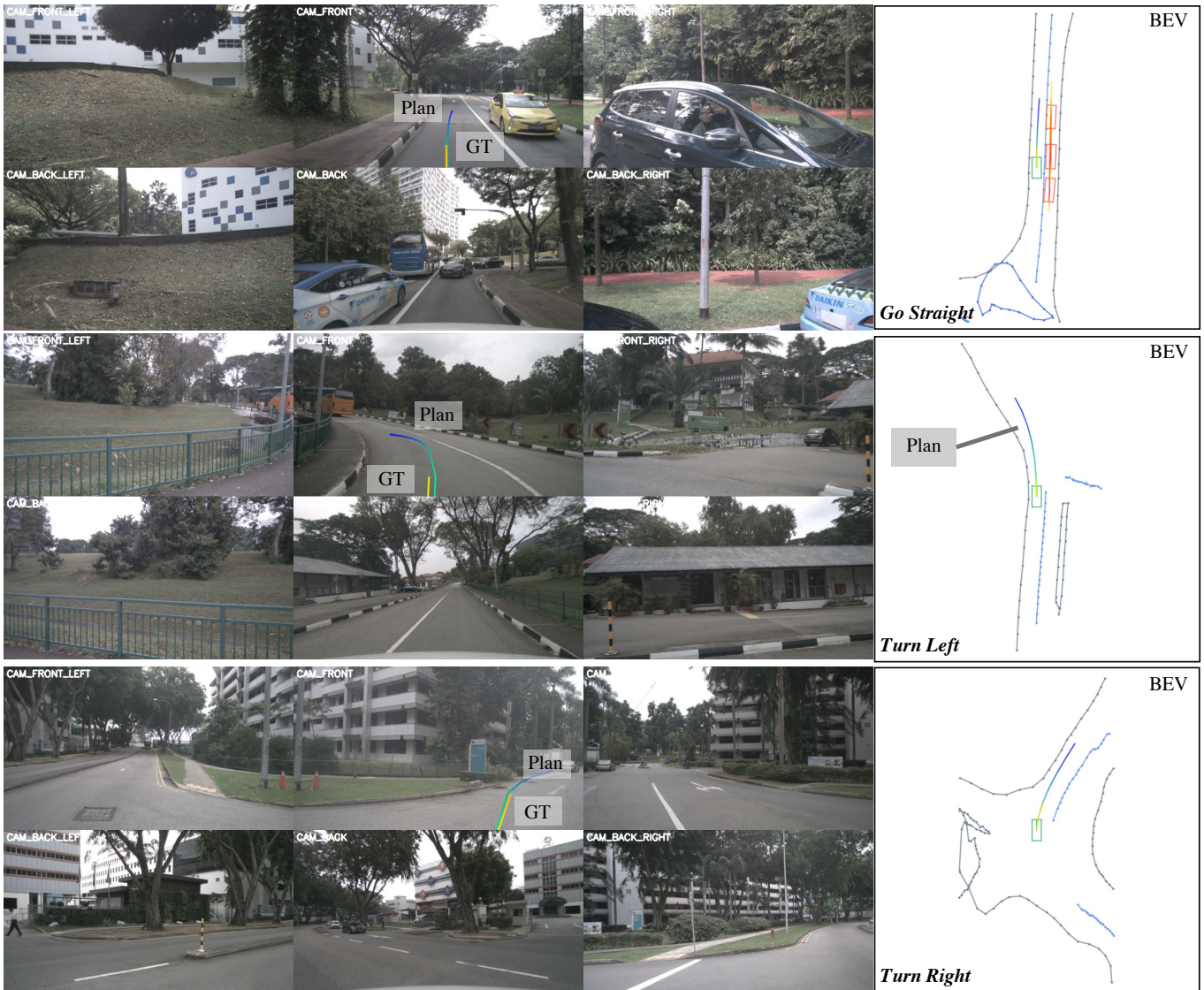


Figure A7. Failure cases of DiFSD with large average L2 error. As can be seen in various scenarios, our DiFSD can make a timely response to different driving commands and plan a more efficient future trajectory of ego vehicle compared with the recorded one of expert driver, considering the driving safety, efficiency and comfortness simultaneously, with the help of the proposed ego-centric fully sparse paradigm.